2024 International Conference on Simulation of Semiconductor Processes and Devices (SISPAD) | 979-8-3315-1635-2/24/$31.00 ©2024 IEEE | DOI: 10.1109/SISPAD62626.2024.10733317

Simulation of Advanced MRAM Devices for sub-ns Switching

Bernhard Pruckner[†,*], Nils Petter Jørstad[†], Mario Bendra[†,‡], Tomáš Hadámek[†],
Wolfgang Goes[§], Siegfried Selberherr[‡], and Viktor Sverdlov[†,‡]
[†] Christian Doppler Laboratory for Nonvolatile Magnetoresistive Memory and Logic at the
[‡] Institute for Microelectronics, TU Wien, Gußhausstraße 27-29, A-1040 Wien, Austria
[§] Silvaco Europe Ltd., Compass Point, St Ives, PE27 5JL, Cambridge, United Kingdom
[*]*Email: pruckner@iue.tuwien.ac.at*

***Abstract*—This work explores pathways to achieve reliable sub-ns switching for Spin-Transfer Torque (STT) and Spin-Orbit Torque (SOT) MRAM devices by employing a coupled spin and charge drift-diffusion and micromagnetics simulation framework utilizing the Landau-Lifshitz-Gilbert (LLG) equation. We consider several vital mechanisms of spin current generation, such as spin current polarization in ferromagnets (FMs), the spin Hall effect (SHE) in heavy metals (HMs), the Rashba-Edelstein effect (REE) at HM/FM interfaces, the magnetic SHE (MSHE) in noncollinear anti-ferromagnets (NC-AFMs), and the anomalous Hall effect (AHE) in FMs. We employ boundary conditions based on quantum mechanical scattering from a magnetic exchange and Rashba SOC potential at the HM/FM interfaces. We also account for all critical effects in the LLG equation, such as the interfacial Dzyaloshinskii-Moriya interaction (DMI), the demagnetizing field, perpendicular magnetic anisotropy, and interlayer exchange coupling (IEC).**

***Index Terms*—Spintronics, SOT-MRAM, STT-MRAM, sub-ns switching**

I. INTRODUCTION

Magnetoresistive random access memory (MRAM) is a non-volatile memory technology, promising nanosecond switching times, high endurance, and high energy efficiency [1], with the potential to replace flash memory, DRAM, and even SRAM in cache memory [2]. The state of the cell is stored through the relative orientation of the magnetization of a perpendicularly magnetized ferromagnetic free layer (FL) and a reference layer (RL) within a perpendicular magnetic tunnel junction (pMTJ), as illustrated in Fig. 1a. The magnetization of the RL is fixed, while the magnetization of the FL can be manipulated via spin currents. The two varieties of MRAM are based on spin-transfer torque (STT), utilizing the spin polarization of the current passing through the RL, and spin-orbit torque (SOT), utilizing spin currents generated in an adjacent heavy metal (HM) layer through spin-orbit coupling (SOC). While STT-MRAM has a smaller footprint and achieves full perpendicular switching, typical switching times are in the 10ns-regime. SOT-MRAM has sub-ns switching speeds. However, to achieve full perpendicular magnetization reversal, typically an additional external field is required, which is detrimental to the density of SOT-MRAM devices.

A double spin torque MTJ (dsMTJ), shown in Fig. 1b, serves as an advanced nonvolatile memory, pushing STT-MRAM technology into the sub-ns regime. dsMTJs rely on a MTJ and a spin valve, consisting of a second RL separated by a nonmagnetic spacer (NMS), on top. This structure leads to additional STT acting in the FL, speeding up the magnetization reversal and enhancing the switching performance twofold, while the TMR remains unchanged compared to that in a regular MTJ [3]. To properly model a multilayer device, IEC acting between the FM layers must be taken into account [4]. IEC is crucial for enhancing memory cell performance and stability in compact MTJ stacks [5]–[7]. In perpendicular SOT-MRAM, the spin currents generated in the HM layer typically have an in-plane polarization. The generation of out-of-plane spin-polarized spin currents, necessary for field-free magnetization switching, has been shown with noncollinear AFMs such as Mn_3Sn [8] and in FM/HM/FM trilayers with interfacial SOC [9]. We investigate the performance of three distinct SOT-MRAM devices, shown in Fig. 2, utilizing (a) the SHE and interfacial SOC in a Pt HM layer, (b) the MSHE in an Mn_3Sn noncollinear AFM layer, and (c) the out-of-plane spin currents in a Co/Pt/CoFeB structure generated due to the trilayer symmetry.

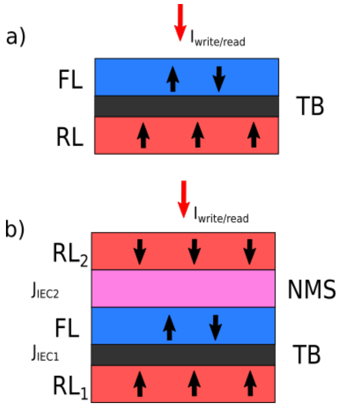

Fig. 1. A sketch of a (a) pMTJ, consisting of a RL and a FL separated by a TB and (b) a dsMTJ with an additional spin valve on top of a pMTJ, consisting of a second RL and a NMS. The IEC strengths between RL_1 and the FL, and between the FL and RL_2 are denoted J_{IEC1} and J_{IEC2}, respectively. The black arrows depict the magnetization of the layers.

We employ our coupled spin and charge drift-diffusion and micromagnetics simulation framework ViennaSpinMag [10], [11]. The finite element method (FEM) is employed for the

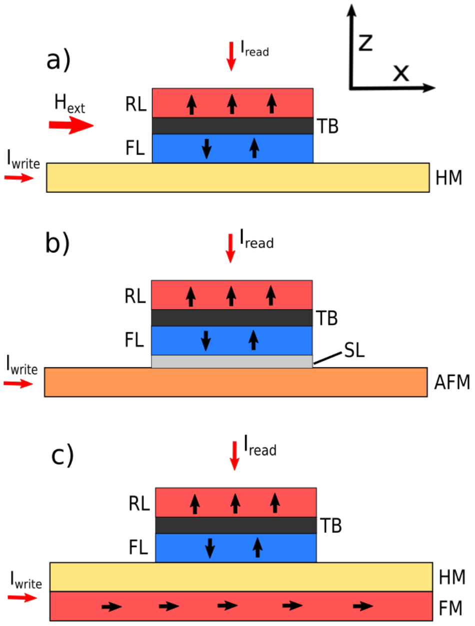

Fig. 2. Three distinct SOT-MRAM cells, consisting of a pMTJ placed on top of an (a) HM-layer, (b) AFM-layer and a nonmagnetic spacer layer (SL) for magnetic decoupling of the AFM and FL layer, and (c) an HM and FM layer, forming an FM/HM/FM trilayer with the adjacent FL. The device depicted in (a) utilizes the SHE and interfacial SOC, the device in (b) utilizes the MSHE, and the device in (c) utilizes spin currents generated due to the symmetry of the trilayer. A charge current is applied in the x-direction.

numerical simulation of the magnetization dynamics, utilizing the Landau-Lifshitz-Gilbert (LLG) equation. In ViennaSpinMag, all important mechanisms of spin current generation are considered: spin current polarization in ferromagnets (FMs), spin Hall effect (SHE) in HMs, the Rashba-Edelstein effect (REE) at HM/FM interfaces, and the magnetic SHE (MSHE) in noncollinear anti-ferromagnets (NC-AFMs). We employ boundary conditions based on quantum mechanical scattering from a magnetic exchange and Rashba SOC potential at the HM/FM interfaces [12], [13], [14]. We also account for all essential effects in the LLG equation, such as the interfacial Dzyaloshinskii-Moriya interaction (DMI), the demagnetizing field, perpendicular magnetic anisotropy [13], and interlayer exchange coupling (IEC).

II. MICROMAGNETIC MODEL

We describe the magnetization dynamics using the LLG equation [15]:

$$\frac{\partial \mathbf{m}}{\partial t} = -\gamma\mu_0 \mathbf{m} \times \mathbf{H_{eff}} + \alpha \mathbf{m} \times \frac{\partial \mathbf{m}}{\partial t} + \frac{1}{M_S}\mathbf{T_S} \qquad (1)$$

$\mathbf{m} = \mathbf{M}/M_S$ is the local normalized magnetization, where M_S is the saturation magnetization. γ is the gyromagnetic ratio, μ_0 is the vacuum permeability, and α is the Gilbert damping factor. The first term describes the precession of the magnetization around the effective field $\mathbf{H_{eff}}$, the second term describes the damping of the magnetization towards $\mathbf{H_{eff}}$, and the third term describes the effect of the spin torque $\mathbf{T_S}$ on the magnetization. $\mathbf{H_{eff}}$ incorporates the magnetic anisotropy field, the exchange field, the demagnetization field, and the IEC contribution. To capture the demagnetization field, a hybrid FEM-Boundary Element Method (FEM-BEM) approach is employed, which combines the boundary element method with the FEM (FEM-BEM) [16]. A complete description of the torque $\mathbf{T_S}$ is obtained from the nonequilibrium spin accumulation $\mathbf{S}$ acting on the magnetization via the exchange interaction and spin-dephasing:

$$\mathbf{T_S} = -\frac{D_e}{\lambda_J^2}\mathbf{m} \times \mathbf{S} - \frac{D_e}{\lambda_\varphi^2}\mathbf{m} \times (\mathbf{m} \times \mathbf{S}) \qquad (2)$$

λ_J is the exchange length, λ_φ is the spin dephasing length, and D_e is the electron diffusion coefficient within the FM layers.

The IEC occurs in layered structures, where a nonmagnetic layer or a TB separates two or more magnetic layers. Various factors, such as the thickness of the nonmagnetic layer and the material can influence the strength and sign of the IEC. The coupling type, ferromagnetic, promoting parallel alignment of the magnetizations, or antiferromagnetic, favoring an antiparallel alignment, depends on the band structure of the spacer layer around the Fermi surface. The IEC over metallic spacers has been explained by the Rudermann-Kittel-Kasuya-Yosida (RKKY) theory [17]. Meanwhile, theories such as variable-range hopping and resonant tunneling through defect-generated localized electronic states in the barrier gap have been developed to explain the more pronounced exponential decay of the exchange coupling strength through semiconducting spacers [18]. For insulating spacers, IEC with appreciable strength and absence of oscillation has been interpreted by spin-dependent tunneling [19], [20]. Incorporating IEC, the free energy density due to interlayer coupling is formulated as:

$$\mathbf{E} = -J\cos(\Delta\phi) \qquad (3)$$

$\Delta\phi$ is the angle between the magnetization directions of the coupled FM layers, with J characterizing the linear coupling constant. Quadratic terms are often attributed to defects such as surface roughness [18], and are therefore neglected. For NMS, J exhibits an oscillatory dependence on the spacer thickness, leading to either ferromagnetic or antiferromagnetic coupling depending on the spacer layer's thickness. For MgO spacers, the coupling is predominantly ferromagnetic and decays exponentially with the thickness of the TB. The IEC contribution leads to an effective field acting at the surface of the FM layers, which contributes to $\mathbf{H_{eff}}$ of the LLG equation [20]. The effective field acting at the surface of a FM layer on one side of the spacer is given by:

$$\mathbf{H_{eff,IEC}} = \frac{J}{\mu_0 M_S}\mathbf{m_{FM}} \qquad (4)$$

$\mathbf{m_{FM}}$ is the magnetization of the FM layer on the opposite side of the spacer layer.

III. SPIN DRIFT-DIFFUSION MODEL

A coupled spin and charge drift-diffusion formalism is used to accurately describe the distribution of the nonequilibrium spin accumulation $\mathbf{S}$. The magnetization dynamics typically happens at a timescale three orders of magnitude slower than that of the spin dynamics [21], and the spin accumulation is assumed to relax to a steady state immediately.

$$\frac{\partial \mathbf{S}}{\partial t} = 0 = -\nabla\cdot\overline{\mathbf{J_S}} - D_e\left(\frac{\mathbf{S}}{\lambda_{sf}^2} + \frac{\mathbf{S}\times\mathbf{m}}{\lambda_J^2} + \frac{\mathbf{m}\times(\mathbf{S}\times\mathbf{m})}{\lambda_\varphi^2}\right) \tag{5}$$

$\overline{\mathbf{J_S}}$ is the spin current density tensor and λ_{sf} is the spin-flip length. The spin current is described by:

$$\overline{\mathbf{J_S}} = -\frac{\mu_B}{e}\beta_\sigma \mathbf{m}\otimes\left(\mathbf{J_C} - \beta_D D_e \frac{e}{\mu_B}\left[(\nabla\mathbf{S})^{\mathbf{T}}\mathbf{m}\right]\right) - D_e\nabla\mathbf{S} \tag{6}$$

$\mathbf{J_C} = \sigma\mathbf{E}$ is the electrical current density from the applied field $\mathbf{E} = -\nabla V$, σ is the electrical conductivity. V is the electrical potential, obtained from solving $\nabla\cdot\mathbf{J_C} = 0$ with Dirichlet boundary conditions for the applied voltage at the contacts. β_D and β_σ are the diffusion and conductivity polarizations, respectively. The first term (6) describes the contribution from polarized currents in ferromagnetic layers, and the second term describes the diffusion of spins.

In SOT-MRAM devices, the spin current is generated in the heavy metal or noncollinear AFM layer, which flows perpendicularly to the applied charge current. In general, the spin current can be described by:

$$\overline{\mathbf{J_S}}_{,SOT} = -\frac{\mu_B}{e}\overline{\theta}_{SCA}\mathbf{J_C} \quad \text{with} \quad \overline{\theta}_{SCA} = \overline{\sigma}_{\mathbf{SH}}\rho \tag{7}$$

$\overline{\theta}_{SCA}$ is the spin-charge angle (SCA) tensor [22], which is a generalization of the scalar spin Hall angle, used to describe the charge-to-spin conversion by the conventional SHE. $\overline{\sigma}_{\mathbf{SH}}$ is the spin Hall conductivity tensor (SHCT) and ρ is the resistivity tensor. In the regular SHE, the SHCT is described by

$$\sigma_{\mathbf{ij}}^{\mathbf{S_k}} = \epsilon_{\mathbf{ijk}}\sigma_{SH}. \tag{8}$$

ϵ_{ijk} is the Levi-Civita tensor and σ_{SH} is the spin-Hall conductivity, which is a single isotropic quantity related to the spin-Hall angle by $\theta_{SHA} = \sigma_{SH}\cdot\rho$ [22]. In the case of the SHE, the nonzero components of the SHCT only generate in-plane spin-polarized spin currents, if the charge current flows parallel to the FM-heavy metal interface. In the MSHE, additional nonzero components of the SHCT generate out-of-plane spin-polarized spin currents.

At HM/FM interfaces, the REE is captured by boundary conditions for the spin current at either side of the interface [13], [14]:

$$\tilde{J}_S^{\text{REE}}\mathbf{n}|_{\text{HM}} = -\frac{\mu_B}{e}\frac{\boldsymbol{\sigma}_{\boldsymbol{S}}^{\mathbf{HM}}(\boldsymbol{m},\boldsymbol{E})}{\sigma}J_C^{\text{ip}} \tag{9}$$

$$\tilde{J}_S^{\text{REE}}\mathbf{n}|_{\text{FM}} = -\frac{\mu_B}{e}\frac{\boldsymbol{\gamma}_{\boldsymbol{S}}^{\mathbf{FM}}(\boldsymbol{m},\boldsymbol{E})}{\sigma}J_C^{\text{ip}} \tag{10}$$

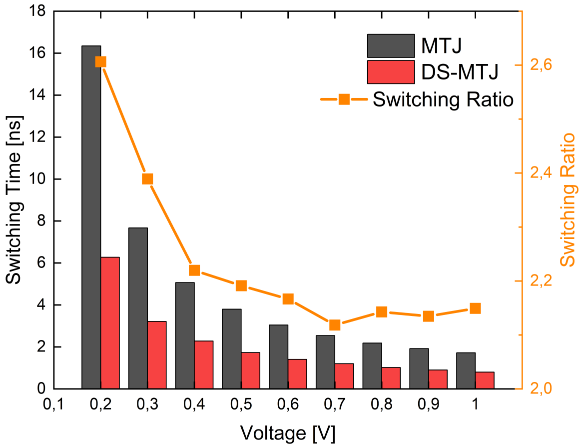

Fig. 3. The switching times for a pMTJ and dsMTJ with a Ru-NMS for different applied voltages. The switching ratio shows the acceleration of the switching process in a dsMTJ device compared to a pMTJ.

J_C^{ip} is the magnitude of the in-plane current at the interface. $\boldsymbol{\sigma}_{\boldsymbol{S}}^{\mathbf{HM}}$ and $\boldsymbol{\gamma}_{\boldsymbol{S}}^{\mathbf{FM}}$ are interfacial conductivity tensors computed by considering quantum mechanical scattering of a Rashba SOC and exchange potential at the interface [13]. The spin currents from the SHE, MSHE, and REE are included as additional contributions to equation (7).

IV. RESULTS

The dsMTJ architecture harnesses additional spin torque coming from the second RL_2, pushing STT-MRAM switching performance to the sub-ns regime [3]. The magnetization direction of the two RLs is anti-parallel. Thus, the STT coming from both RLs adds up, leading to an increase in total torque acting in the FL. Fig. 3 depicts the enhancement of the switching performance of the dsMTJ device with a Ru NMS compared to a regular MTJ. Due to the additional torque coming from the second RL, a twofold increase in switching speed can be observed.

The IEC coupling, J_{iec_1} and J_{iec_2} as depicted in Fig. 1b, reveals their significant impact on switching dynamics, underscoring the potential to accelerate magnetization reversal, as detailed in Fig. 4, for a dsMTJ with a Ru-NMS. Negative coupling constants correspond to AFM coupling and positive ones to FM coupling.

While a regular SHE-driven SOT-MRAM device needs an additional external field to achieve field-free switching, the device based on the MSHE in a Mn_3Sn layer, as well as a device utilizing a FM/HM/FM trilayer, achieves fully perpendicular sub-ns switching without the need for an additional external magnetic field. This behavior can be explained by studying the spin currents, shown in Fig. 6. Both the Mn_3Sn/CoFeB bilayer through the MSHE (a) and the Co/Pt/CoFeB trilayer through its symmetry (b) generate out-of-plane spin-polarized spin currents along the z-axis (shown in green) when an in-plane charge current is applied, which facilitate perpendicular magnetization switching. Fig. 5 shows the thickness dependence of the spin currents produced in the bilayer and trilayer

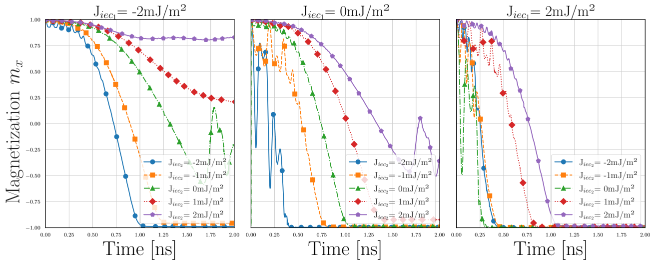

Fig. 4. The magnetization dynamics in a dsMTJ device with a Ru NMS during switching from a P to an AP state, emphasizing the critical role of the IEC parameters J_{IEC_1} and J_{IEC_2}. The analysis mirrors experimental insights into magnetic coupling. The left section shows the effect of a negative J_{IEC_1}, the middle with J_{IEC_1} at zero for comparison, and the right with a positive J_{IEC_1}.

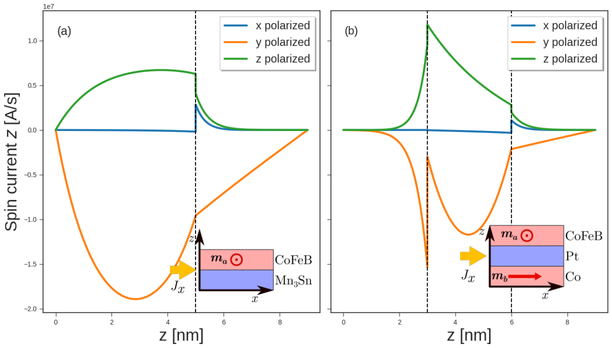

Fig. 5. The spin currents generated in (a) a Mn$_3$Sn(5nm)/CoFeB(4 nm) bilayer with a 2×10^{12} A/m^2 in-plane electric current and (b) in a Co(3 nm)/Pt(3 nm)/CoFeB(3 nm) trilayer with a 5×10^{12} A/m^2 in-plane electric current, and interfacial SOC at the Co/Pt interface. The magnetization directions are depicted in the insets.

structures, as well as the ratio of out-of-plane/in-plane spin currents. A large ratio is beneficial to field-free perpendicular magnetization switching efficiency.

Fig. 7 shows the switching performance for perpendicular magnetization reversal of the SOT-devices depicted in Fig. 2. The MSHE-driven device can compete with the conventional SHE-driven device in terms of switching speed. This is achieved without an external magnetic field. The device utilizing the trilayer symmetry shows an even better switching performance clearly. Both, the MSHE-driven device and the trilayer device show clear sub-ns switching for current densities that have also been reported experimentally.

In conclusion, with our coupled drift-diffusion and micromagnetic approach utilized in the ViennaSpinMag simulator, we can account for considerably relevant phenomena in STT- and SOT-MRAM devices. Through simulations of the magnetization dynamics, we have shown that with the dsMTJ + IEC approach, the STT-MRAM performance can be boosted into the sub-ns switching regime. Moreover, we also demonstrate field-free sub-ns switching in SOT-MRAM based on the MSHE and FM/HM/FM trilayers, proving the potential for MRAM in the last-level cache application.

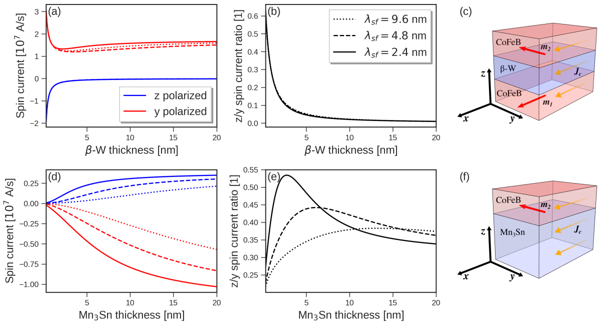

Fig. 6. Thickness dependence of the average spin polarization current density (a,d), and z/y spin current polarization ratio (b,e), for a CoFeB(4 nm)/β-W(t)/CoFeB(1.2 nm) trilayer (a-b) and Mn$_3$Sn(t)/CoFeB(1.2 nm) bilayer (d-e), depicted in (c) and (f), respectively. We consider the SHE in β-W, a strong REE at β-W/CoFeB interfaces, and MSHE in Mn$_3$Sn. An 1×10^{12} A/m^2 in-plane electrical current density drives the out-of-plane spin currents.

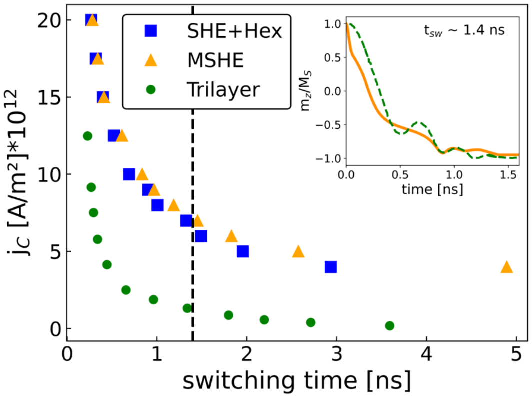

Fig. 7. Switching performance of the SOT devices shown in Fig. 2, utilizing the regular SHE and an additional external field, the MSHE, and the trilayer symmetry. The inset shows the normalized z-component of the magnetization of the devices utilizing the MSHE (orange) and the trilayer symmetry (green) for current densities indicated by the vertical black line.

REFERENCES

[1] T. Y. Lee, et al., in: IEDM, 2022, pp. 10.7.1–10.7.4.
[2] R. Saha, et al., J. Magn. Magn. Mater. 551 (2022) 169161.
[3] B. Pruckner, et al., Physica B: Condensed Matter 688 (2024) 416124.
[4] M. Bendra, et al., Micromachines 15 (2024) 568.
[5] S. K. Patel, et al., Spin. Mag. Nano. 8 (2023) 201–210.
[6] G. Hu, et al., in: IEDM, 2021, pp. 2.5.1—2.5.4.
[7] M. Bendra, et al., in: Devices Research Conference (DRC), 2024.
[8] S. Hu, et al., Nat. Commun. 13 (2022) 4447.
[9] J. Ryu, et al., Nature Electronics 5 (2022) 217–223.
[10] S. Fiorentini, et al., Sci.Rep. 12 (2022) 20958.
[11] CDL NovoMemLog, ViennaSpinMag, last accessed on 30 March 2023. URL `https://www.iue.tuwien.ac.at/viennaspinmag/`
[12] V. P. Amin, et al., J. Appl. Phys. 128 (2020) 151101.
[13] N. Jørstad, et al., Physcia B: Condensed Matter 676 (2024) 415612.
[14] V. P. Amin, et al., Phys. Rev. B 94 (2016).
[15] J. Xiao, et al., Phys. Rev. B 72 (2005) 014446.
[16] J. Ender, et al., in: 2020 International Conference on Simulation of Semiconductor Processes and Devices (SISPAD), 2020, pp. 213–216.
[17] M. A. Ruderman, et al., Phys. Rev. 96 (1954) 99–102.
[18] P. Bruno, et al., Journal of Physics: Condensed Matter 11 (1999) 9403–9419.
[19] K. Inomata, et al., Phys. Rev. Lett. 74 (1995) 1863–1866.
[20] M. Chshiev, et al., Phys. Rev. B 92 (2015).
[21] S. Zhang, et al., Phys. Rev. Lett. 88 (2002).
[22] L. Salemi, et al., Phys. Rev. B 106 (2022) 024410.